A Three-dimensional Analytical Framework for Retinal Microvasculature Reveals Layer-associated Vulnerability in Development and Neovascular Remodeling

Wenhao Shang, Guiying Hong, William E. Keller, Ryan A. Morton, Pierre Zeboulon, Toma Kenichi, Xin Duan, Douglas B. Gould, Tyson N. Kim

Abstract

The neurosensory retina is one of the most metabolically active tissues in the body and a uniquely accessible extension of the central nervous system, where neuronal and vascular structures can be visualized non-invasively. Its accessibility and highly organized laminar architecture make it a powerful model for studying vascular development and a window into systemic health. Although computational analyses of retinal images have enabled risk assessment for ocular and systemic diseases, most vascular studies rely on two-dimensional frameworks with limited resolution of capillary structure and layer-specific organization. Here, we present a high-resolution three-dimensional (3D) imaging and analysis pipeline enabling quantification of retinal microvasculature and extraction of structural and network metrics across vascular layers. We apply this approach to two mouse models of aberrant retinal vascular development: one with spontaneous postnatal chorioretinal neovascularization and another with disrupted neurovascular lattice formation and layered organization in early life. Across both pathologic contexts, 3D analysis enables detailed characterization of retinal vascular architecture and identifies early vulnerability within the intermediate plexus, the vascular network that bridges the superficial and deep retinal layers, as a sensitive indicator of abnormal remodeling and neovascularization. This framework enables precise characterization of retinal vasculature and establishes a foundation for identifying new retinal biomarkers with potential relevance to neurovascular and systemic disease.

Introduction

The retina provides a unique opportunity to study the central nervous system *in vivo*. As a direct extension of the brain, it enables non-invasive, high-resolution visualization of neural and vascular networks in their native physiological context. The mammalian retina is among the most metabolically active tissues in the body, containing hierarchical vascular plexuses arranged in parallel planes and interconnected by orthogonal penetrating vessels.[1] This combination of structure and imaging accessibility has made the retina both a benchmark model for vascular development and a powerful window into systemic health. A growing body of evidence demonstrates that retinal vascular abnormalities provide quantitative biomarkers in identifying and monitoring cardiovascular and neurological diseases.[2,3] Advances in computational and deep learning approaches have revealed that retinal vascular features captured in fundus images can predict systemic disease risk with accuracy comparable to clinical assessment.[4] Further work has identified markers of cerebral small vessel diseases within the deeper retinal plexus,[5] highlighting the relevance of pathologic features amid specific retinal layers. As imaging and analytical methods advance, a deeper understanding of the retina's three-dimensional (3D) microarchitecture is poised to illuminate fundamental links between ocular, cerebral, and systemic health.[6]

Most retinal vascular analyses rely on two-dimensional (2D) approaches without depth resolution and primarily focus on macrovascular structures using conventional imaging such as fundus photography.[7] By projecting all retinal layers onto a single plane and emphasizing larger vessels, these analyses can obscure microvascular alterations specific to the retina's layers, each with distinct functional and metabolic demands. Optical coherence tomography angiography (OCTA) has emerged as a powerful tool for non-invasive, depth-resolved

visualization of the retinal vasculature, enabling 3D mapping of the superficial and deep plexuses.[8,9] Ongoing advances in OCTA-based reconstruction and quantification have begun to capture finer vascular detail, though current analyses remain largely focused on vessel-level metrics with limited representations of the intermediate plexus and inter-layer connectivity.[10–13] Complementary advances in high-resolution optical techniques, particularly multiphoton microscopy, extend this capability by achieving *in vivo* visualization of structural and dynamic biological processes such as neovascularization, perfusion, and blood-flow dynamics within the retina with subcellular resolution,[14–16] serving as an imaging benchmark for high-resolution analysis in animal models. Multiphoton microscopy achieves this by simultaneous absorption of two or more lower-energy photons, typically in the near-infrared range. The use of longer excitation wavelengths reduces light scattering and phototoxicity, while the nonlinear dependence of fluorescence on excitation intensity confines signal generation to the focal volume. These properties confer intrinsic optical sectioning in 3D and allow imaging at subcellular resolution to depths not accessible by conventional microscopies.[17–19] A growing number of studies demonstrate the importance of high-resolution 3D imaging for capturing fine architectural features in the retina,[20,21] yet quantitative frameworks to characterize these complex 3D networks and architectures remain limited.[22–24] While computational tools for automated vascular network quantification have been developed, including 2D frameworks such as AngioTool[25] and recent 3D approaches for deep learning-based segmentation and morphometric extraction[26] or graph-based analysis of pre-segmented vasculature,[27] these methods have primarily focused on vessel-level morphometrics (density, length, radius) and additional work is needed to address layer-resolved architecture, inter-plexus connectivity, or fractal complexity within individual vascular compartments. Advancing such 3D analytical methods will be valuable for capturing the retina's layer-specific organization, inter-plexus

connectivity, and topological complexity that provides deeper insight into vascular development, disease mechanisms, and potential biomarkers of retinal and systemic disorders.

The retinal vasculature comprises three distinct and highly organized plexus layers that precisely regulate blood flow and nutrient delivery to meet the retina's high metabolic demands.[28,29] Each layer exhibits unique structural and functional characteristics, as well as vulnerability across disease states. Despite this recognized layer-specific vulnerability, quantitative characterization of the intermediate capillary plexus has been limited, in part because most imaging and analytical frameworks struggle to resolve this compartment as an independent entity.[3,30] Quantifying structural changes within and between these layers may yield nuanced insights into vascular development and disease pathology. Our recent work with Toma et al. demonstrated that the development of these inter-plexus vessels is regulated by a subpopulation of perivascular retinal ganglion cells (RGCs) through direct neuron-vessel contact.[31] Prior studies have shown that these vertical vessels also arise predominantly from veins and capillaries, underscoring their distinct developmental origin.[32] To systematically investigate such complex spatial and functional relationships, we developed a comprehensive 3D quantification framework that extracts detailed structural metrics from high-resolution imaging data, enabling quantitative analysis of retinal vascular organization across multiple layers and their interconnectivity. This framework has provided new insight into neurovascular patterning and dysgenesis, including the discovery of a novel mechanism of vascular development in the retina whereby specialized neurons guide 3D vascular lattice organization mediated through direct neuron-vessel contact.[31] Here, we extend this framework to resolve distinct mechanisms of 3D vascular remodeling in the retina, applying it in two representative contexts relevant to development and disease: (i) spontaneous chorioretinal neovascularization in postnatal life and (ii) disrupted 3D vascular lattice formation in the developing retina.

Results

A pipeline for 3D retinal vasculature analysis

We developed an end-to-end pipeline for analyzing 3D retinal vasculature, which reconstructs full-thickness networks from high-resolution image Z-stacks through computer-aided segmentation, yielding detailed computational representations of the 3D vascular architecture (Fig. 1a–c). The reconstructed networks are subsequently stratified into anatomically distinct layers: the superficial layer plexus (SL), middle layer plexus (ML), and deep layer plexus(DL), along with identification of their inter-plexus connections (Fig. 1c,d).

Following reconstruction and layer stratification, we established a multi-level quantification framework that systematically characterizes retinal vascular metrics across different organizational scales. Our approach integrates three complementary analytical modules: (i) full-thickness analysis capturing global network properties, (ii) plexus-specific quantification revealing layer-dependent features, and (iii) inter-layer connectivity analysis characterizing cross-plexus organization, a dimension largely unexplored in previous studies. At the full-thickness and individual plexus levels, we quantify standard morphometric and topological parameters including vessel segment length, diameter, tortuosity, vessel volume density, vessel number density, and branching point density (Fig. 1b-c). In addition to these conventional metrics, we incorporate 3D fractal dimension (3D FD) to capture geometric complexity and introduce layer-specific parameters, such as the fragmentation index, to assess network characteristics.

For inter-layer connectivity analysis, we developed metrics specifically designed to quantify cross-plexus organization: (i) inter-layer parallelism, measuring the degree of parallel alignment between vascular plexuses; (ii) inter-plexus connection classification, categorizing and quantifying different connection types between specific vascular layers (DL–ML, SL–ML,

DL–SL); and (iii) inter-plexus vessel geometries, characterized by excursion ratio (vessel path length normalized to vertical span) and orientation angle θ relative to the retinal plane (Fig. 1d). These metrics enable systematic detection of alterations in vertical vessel architecture and inter-layer coordination. All analyses can be performed across entire vascular territories or within user-defined regions of interest (ROI), providing flexible spatial resolution for both global assessments and targeted investigation within specific vascular domains. A comprehensive catalog of quantification parameters and their definitions is provided in Table 1. The description of the analytical workflow, including image acquisition through 3D reconstruction to multi-level quantification, is illustrated in Fig 1.

3D structural analysis of spontaneous chorioretinal neovascularization and anastomoses reveals capillary rarefaction, ML fragmentation, and radialization of DL vessels

We evaluated an established model of chorioretinal neovascularization, wherein mice harboring a missense point mutation of type-IV collagen (Col4a1$^{+/\Delta ex41}$) develop neovascularization and chorioretinal anastomoses (CRA) in postnatal life. These mice represent a robust genetic model of spontaneous chorioretinal neovascularization,[33] providing a platform for interrogating the 3D structural features of pathologic angiogenesis in the adult eye.

3D image data of the chorioretinal vasculature were acquired from three experimental groups: littermate controls, mutant mice not exhibiting neovascular lesions (Col4a1$^{+/\Delta ex41}$), and mutant mice harboring neovascular changes and CRA (Col4a1$^{+/\Delta ex41}$+CRA). Following vascular segmentation of raw image data, we performed full-thickness network analysis and quantification of vascular characteristics within a standardized region of interest (ROI; 285 × 285 μm, matching the mean CRA lesion size; Fig. 2a, c) spanning the complete retinal vascular thickness from choroid to superficial layer plexus, ensuring consistent spatial sampling across

143 eyes for downstream quantitative analyses. Geometric characterization at the full-thickness
144 level revealed profound vascular remodeling in the Col4a1$^{+/\Delta ex41}$+CRA group. Vessels
145 exhibited significantly larger mean diameters (CRA: 7.47 ± 3.31 μm vs. control: 3.77 ± 1.74
146 μm; $p<0.0001$; Fig. 2d) and increased vessel volume density (Fig. 2e) compared with both
147 control and Col4a1$^{+/\Delta ex41}$ groups. In contrast, vascular network connectivity was markedly
148 compromised, with vessel number density reduced by 72% (CRA: 4.88 ± 2.62 vs. control:
149 17.41 ± 10.79 $\times 10^{-4}/\mu m^3$; $p<0.05$; Fig. 2f) and similar reductions in branching point density
150 (Fig. 2g). To quantify microvascular architectural complexity, we computed the 3D fractal
151 dimension (3D FD) of vascular surfaces using the Bouligand–Minkowski method (see
152 Methods).[34] The Col4a1$^{+/\Delta ex41}$+CRA group exhibited significantly elevated 3D FD (1.86 ± 0.08)
153 compared with control (1.68 ± 0.09) and Col4a1$^{+/\Delta ex41}$ mice (1.67 ± 0.06), representing an ~11%
154 increase ($p<0.05$ for both comparisons; Fig. 2h). Additional morphometric metrics, including
155 vessel segment count, branching points, total vessel length, mean segment length, and vessel
156 straightness are provided in Supplementary Fig. S1. This elevation reflects greater surface
157 irregularity and volumetric complexity, which we find to be characteristic of pathological
158 neovascular structures.

159 We identified two key structural domains in large CRA: a lesion core marked by loss of the
160 retina's trilaminar vascular architecture and aberrant choroid-to-retina vascular connections,
161 and a surrounding peripheral region with disorganization of the retina's three-layer network
162 (Fig. 2i, j). Notably, the ML was completely absent within the CRA core and highly fragmented
163 in the peripheral regions surrounding the lesion (Fig. 2j, k, l). Quantification also revealed that
164 the ML fragmentation index in Col4a1$^{+/\Delta ex41}$ retinas (10.14 ± 1.63 fragments/mm²) was
165 significantly elevated compared with controls (5.44 ± 1.20 fragments/mm²), representing an
166 86% increase ($p<0.05$; Fig. 3h). This pattern of ML disruption, with complete loss centrally
167 and progressive fragmentation peripherally, suggests a spatial gradient of vulnerability

168 radiating from the neovascular focus. CRA lesions also exhibited a distinctive tree-like
169 configuration in which a small number of large choroidal anchor vessels gave rise to branches
170 with radial orientation that integrated into all layers of the retinal vasculature (Fig. 2i). This
171 architecture was accompanied by abnormally narrow vessel bifurcations, wherein branching
172 angle (β) within CRA were significantly smaller than those in surrounding non-CRA
173 vasculature (Fig. 2m). Notably, β of non-CRA vasculature in mutants did not differ
174 significantly from controls, suggesting that the shift toward lower β values can provide a unique
175 biomarker that helps identify and distinguish these aberrant neovessels as they merge into the
176 pre-existing retinal plexuses.

177 To identify architectural abnormalities that emerge before overt neovascular lesions form, we
178 performed layer-resolved analysis comparing control and pre-neovascular Col4a1$^{+/\Delta ex41}$ retinas.
179 Following manual stratification of the reconstructed networks into anatomically distinct layers
180 (SL, ML, and DL) with comprehensive mapping of all inter-plexus connections (Fig. 3a–f, m',
181 n'), we conducted layer-specific 3D fractal dimension (FD) analysis and geometric
182 quantification.

183 Initial 3D FD screening revealed that the ML and inter-plexus connections exhibited the most
184 pronounced structural alterations. 3D FD of the ML was significantly elevated in Col4a1$^{+/\Delta ex41}$
185 retinas compared with controls (FD: 1.87 ± 0.07 vs. 1.61 ± 0.03, $p<0.05$; Fig. 3k). In contrast,
186 the DL and SL showed no significant changes in fractal complexity (Fig. 3j, l), indicating that
187 early structural remodeling is compartmentalized to the ML. Layer-level structural comparison
188 revealed distinct connectivity alterations in the ML. While control ML networks formed
189 continuous, hierarchically organized meshes with interconnected vessel segments (Fig. 3b),
190 Col4a1$^{+/\Delta ex41}$ ML vessels appeared predominantly as disconnected fragments (Fig. 3e). This
191 architectural disruption was quantitatively confirmed by 80% increase in ML fragmentation

index (p<0.05; Fig. 3h), indicating substantial loss of network connectivity prior to neovascularization. Layer parallelism analysis revealed selective disruption of ML alignment in Col4a1$^{+/\Delta ex41}$ retinas. While control retinas maintained near-perfect parallel alignment across all layers (DL and ML deviation ~5°; Fig. 3m), Col4a1$^{+/\Delta ex41}$ retinas showed significant ML misalignment (8.0 ± 1.9° vs 5.1 ± 1.2° in controls, p<0.05). Point-wise parallelism mapping revealed spatial heterogeneity in both layers (Fig. 3m, m'), but only the ML demonstrated statistically significant architectural disruption (Fig. 3m″), identifying the ML as the primary site of early layer disorganization in pre-neovascular retinas. Quantification of inter-plexus connections revealed a disease-specific shift in cross-layer connectivity patterns. While DL-ML and SL-ML connections predominated in both groups, Col4a1$^{+/\Delta ex41}$ retinas showed a significant 3.5-fold increase in DL-SL direct connection density (63 ± 17 vs. 18 ± 10 connections per μm²; p<0.001; Fig. 3n″), with corresponding increases in vessel length per unit area. This compensatory re-routing between deep and superficial layers likely reflects adaptive responses to ML disruption. Together, these multi-scale analyses highlight the ML and inter-plexus connections as particularly sensitive compartments that undergo substantial architectural remodeling prior to overt neovascularization, with changes detectable through fragmentation, layer misalignment, and altered cross-layer connectivity patterns.

Neuronal loss of Piezo2 disrupts 3D retinal vascular lattice development with selective alterations in the ML and inter-plexus connectivity.

Neurovascular patterning of the retinal 3D vascular lattice depends on the coordinated development of planar vascular plexuses and the penetrating vessels that interconnect them. Our recent work with Toma et al[31] established that a specialized subset of perivascular retinal ganglion cells (Nts-RGCs) guides the development of penetrating vessels through a Piezo2-dependent contact mechanism during retinal development. Motivated by this paradigm, we

216 used Nts-RGC-specific Piezo2 knockout mice (Piezo2^{Nts}) to evaluate whether our 3D
217 quantification pipeline could sensitively detect developmental patterning defects and to
218 determine how loss of neuron-derived mechanosensory cues alters plexus-resolved vascular
219 architecture.

220 At the full-thickness scale, Piezo2^{Nts} retinas exhibited modest but significant increases in mean
221 vessel diameter compared with controls (9.0 ± 2.0 vs. 6.8 ± 1.5 μm, $p<0.05$; Fig. 4b), with
222 trends toward altered vessel volume density and branching point density (Fig. 4c, d). Full-
223 thickness 3D fractal dimension (FD) analysis revealed a subtle but significant elevation (1.95
224 ± 0.03 vs. 1.91 ± 0.02, $p<0.05$; Fig. 4e), suggesting early increases in vascular surface
225 irregularity and disruption of 3D lattice formation. Additional full-thickness metrics, including
226 retinal thickness, convex hull volume, vessel segment count, total vessel length, mean segment
227 length, and vessel straightness are provided in Supplementary Fig. S3.However, these full-
228 thickness measurements obscured the compartment-specific architectural abnormalities that
229 drive the phenotype, underscoring the critical importance of layer-resolved quantitative
230 analysis.[35] We separately evaluated SL, DL, and intermediate plexus (IP), where the IP
231 encompasses the ML vessels and penetrating connections that develop and undergo active
232 remodeling during the early postnatal period. Consistent with the temporal sequence of retinal
233 vascular lattice assembly and the known role of Nts-RGCs in guiding penetrating vessel
234 orientation, Piezo2 loss selectively and profoundly impaired IP organization while sparing the
235 earlier-formed planar plexuses. Layer-resolved 3D FD analysis immediately identified the IP
236 as the primary site of structural disruption. IP-specific FD was markedly elevated in Piezo2^{Nts}
237 retinas (1.71 ± 0.04 vs. 1.63 ± 0.02, $p<0.01$; Fig. 4h), whereas DL and SL showed no significant
238 changes (Fig. 4g, i). This compartmentalized complexity increase was accompanied by
239 profound alterations in IP vessel geometry and connectivity. IP vessels displayed significantly
240 larger mean segment diameters (8.5 ± 2.0 vs. 6.8 ± 1.5 μm, $p<0.0001$; Fig. 4h') and a striking

241 40% increase in fragmentation index (1.28 ± 0.15 vs. 0.90 ± 0.15 ×10^3 fragments/mm^3, $p<0.05$;
242 Fig. 4h"), indicating substantial disruption of intermediate layer network integrity. In contrast,
243 while the SL and DL exhibited modest diameter increases, neither layer showed significant
244 changes in network fragmentation or fractal complexity (Fig. 4g, i), supporting the
245 interpretation that IP assembly represents a particularly vulnerable developmental program
246 during the coordinated 2D to 3D vascular transition of the retina. Per-plexus analyses of
247 additional morphometric parameters, including vessel segment count, branching points, total
248 vessel length, mean segment length, and vessel straightness confirmed that these metrics did
249 not differ significantly between genotypes in any layer (Supplementary Fig. S4), further
250 supporting the specificity of IP disruption to fractal complexity, vessel diameter, and network
251 fragmentation.

252 We further examined inter-layer connectivity by analyzing the geometry of penetrating vessels
253 that join adjacent vascular plexuses. For each penetrating vessel, we defined the orientation
254 angle (θ) as the deviation between the straight-line vector connecting its fusion points across
255 plexuses and the axis orthogonal to the plexus planes (Fig. 4l, m). To quantify deviation from
256 an ideal vertical trajectory, we calculated the excursion ratio (ER), defined as the ratio of the
257 vessel's true path length (L) to the orthogonal inter-plexus distance (D), where values
258 approaching 1.0 indicate direct routing and higher values reflect tortuous or oblique trajectories.
259 Piezo2^{Nts} retinas exhibited a pronounced shift toward oblique penetrating vessel trajectories.
260 Mean orientation angles were significantly increased compared with controls (θ: 49.8 ± 10.7°
261 vs. 27.6 ± 8.3°, $p < 0.001$), and penetrating vessels followed substantially longer and less direct
262 paths, as reflected by elevated excursion ratios ($\log_{10}$(ER): 1.91 ± 0.24 vs. 1.26 ± 0.17, $p <$
263 0.001; Fig. 4l). These changes indicate a transition from compact, near-orthogonal trajectories
264 toward elongated and highly oblique courses spanning the inter-plexus space.

To evaluate how these geometric features covary, we paired θ and $\log_{10}$(ER) for each penetrating vessel and constructed two-dimensional probability density distributions across inter-plexus classes (SL-DL, DL-ML, SL-ML, and combined). In Piezo2^{Nts} retinas, joint distributions were consistently shifted upward and rightward relative to controls, with density contours extending into higher-angle and higher-excursion regimes (θ ≈ 40–70°, $\log_{10}$(ER) ≈ 1.6–2.3; Fig. 4l–o). In contrast, control distributions remained tightly concentrated within lower-angle, lower-excursion domains (θ ≈ 10–30°, $\log_{10}$(ER) ≈ 1.0–1.4), consistent with well-aligned, vertically oriented penetrating vessels.

Stratification by connection subtype revealed that SL–DL and SL–ML vessels exhibited the most pronounced rightward and upward displacements in θ-ER space, together with broader contour spread, indicating both increased deviation and variability in penetrating vessel geometry (Fig. 4m, o). These connection types, originating from or terminating at the superficial plexus anatomically accessible to Nts-RGC somata and dendrites, displayed the most severe geometric perturbations and loss of stereotyped precision. In contrast, DL-ML connections showed comparatively smaller shifts (Fig. 4n), consistent with reduced Nts-RGC contact.

These findings demonstrate that Piezo2-dependent neuronal guidance is essential for establishing proper vertical scaffolding architecture and intermediate layer plexus organization during postnatal development. Notably, this IP-centered disruption in Piezo2^{Nts} retinas mirrors the vulnerability observed in the neovascularization model, where early ML disorganization precedes overt lesion formation. This convergence across developmental and pathological contexts underscores a shared susceptibility of the ML to distinct biological insults and highlights the sensitivity of our 3D quantitative framework for detecting common structural mechanisms underlying retinal vascular remodeling.

Discussion

The neurovascular retina is a uniquely accessible extension of the central nervous system, enabling direct visualization of its vascular network and exquisitely organized laminar architecture. This combination of accessibility and structural precision has established the retina as a powerful model for studying vascular development and a promising window into systemic and neurovascular health. In this study, we establish a framework for detailed 3D retinal vascular quantification and demonstrate its ability to resolve overt pathology and subtle pre-pathological remodeling across distinct biological contexts. Applying this framework to models of spontaneous chorioretinal neovascularization in adult eyes and disrupted 3D neurovascular lattice formation during early retinal development, we provide quantitative insight into these processes and uncover a convergent vulnerability of the ML that emerges early, before overt neovascularization or architectural failures of the retinal vasculature.

Our approach demonstrates high sensitivity beyond conventional vessel-level metrics by resolving network and layer-specific architectural changes. In a pathological angiogenic setting, analysis of Col4a1$^{+/\Delta ex41}$ retinas enabled robust detection and characterization of spontaneous chorioretinal neovascularization, capturing hallmark features of disease, including vessel enlargement, capillary rarefaction, and increased morphologic complexity. Importantly, the framework also revealed architectural abnormalities extending beyond established lesion cores, including early fragmentation and misalignment of the ML and altered inter-plexus routing. These changes were also detectable prior to overt neovascularization, indicating that 3D microarchitectural disruption may represent an early marker of vascular instability rather than just a secondary consequence of formed lesions. The spatial gradient of ML loss, ranging from complete absence within lesion cores to progressive fragmentation in surrounding regions, supports a model in which failure of the middle plexus serves as an organizing feature of chorioretinal neovascular disease. This preferential vulnerability of the intermediate plexus

aligns with emerging clinical evidence. Recent OCTA studies in diabetic retinopathy have demonstrated that the intermediate capillary plexus exhibits distinct and early density reductions that predict disease progression,[30] and that capillary nonperfusion in the deeper plexuses is associated with both photoreceptor disruption and functional visual loss.[36] These clinical observations, together with anatomical studies revealing the unique connectivity architecture of the IP in human retinas,[37] support the notion that this vascular compartment occupies a structurally and functionally vulnerable position within the retinal vascular hierarchy. By contrast, during early retinal development, loss of Piezo2 in Nts-RGCs disrupted retinal vascular organization by impairing neurovascular guidance rather than causing pathological angiogenesis, producing a similarly profound but developmentally driven alteration of ML architecture. Although full-thickness metrics suggested only modest alterations, layer-resolved analysis revealed profound disruption of the intermediate plexus and its penetrating connections. Increased fragmentation, elevated fractal complexity, and geometric distortion of interplexus vessels point to failure of the vertical vascular scaffold that normally integrates planar plexuses into a coherent 3D lattice. These findings refine our prior work by demonstrating that Piezo2-dependent neuronal guidance is not merely required for penetrating vessel emergence, but is essential for preserving IP integrity during the critical developmental transition from planar to fully 3D vascular organization.

Oculomics is the quantitative assessment of ocular imaging features to derive imaging-based biomarkers of systemic, cardiovascular, and neurological disease.[38,39] Prior studies of retinal vasculature have identified important indicators of systemic and neurological disorders using fundus photography and fluorescein angiography.[4,40] More recently, OCT angiography has enabled depth-resolved visualization and separation of retinal vascular plexuses; however, most downstream quantitative analyses have relied on simplified 2D vascular representations

338 and vessel metrics such as vessel caliber, density, tortuosity, and 2D fractal dimension.[41–43]
339 Deep learning approaches have further leveraged these representations, demonstrating
340 encouraging performance for detecting biomarkers of cardiovascular[44] and neurological
341 disorders,[45,46] including Alzheimer's disease[47] and cognitive impairment.[48,49] Despite these
342 advances, reliance on reduced 2D representations may obscure critical aspects of vascular
343 network organization inherent to the retina's 3D architecture. Leveraging fully 3D vascular
344 representations, including layer-specific architecture and inter-plexus connectivity, therefore
345 represents a critical opportunity to expand the biomarker space and advance the field of
346 oculomics. In this study, we demonstrate that 3D, interlayer, and layer-specific analyses reveal
347 subtle vascular alterations. We found the 3D fractal dimension to be an informative readout, as
348 it implicitly captures network complexity, tortuosity, and layer curvature, which may be lost in
349 2D analyses.[50] Our 3D analytical pipeline further enables the characterization of complex
350 vascular phenotypes, such as CRAs, in which aberrant and neovascular structures traverse
351 multiple retinal layers. This approach captures true spatial vascular trajectories and interlayer
352 relationships, including the absence of the ML within CRA lesion cores and its fragmentation
353 in the CRA periphery. Notably, both the Col4a1$^{+/\Delta ex41}$ and Piezo2^{Nts} mouse models evaluated
354 in this study exhibit previously reported cerebrovascular abnormalities,[31,33,51,52] supporting the
355 link between retinal and cerebrovascular irregularities across disease contexts. Together, this
356 work provides a framework for comprehensive 3D retinal vascular analysis that will facilitate
357 future studies linkaging retinal microvascular organization with systemic and neurovascular
358 pathology.

359 This study has several important limitations. Although the analytical framework we present is
360 broadly applicable, the work described here presents a focused subset of analytical outputs, as
361 we deliberately concentrated on metrics that were informative for the disease contexts

examined. Several sub-analyses currently require manual parameter tuning, and vessel segmentation is only partially automated, necessitating manual verification and refinement; these steps can be time-intensive and highlight clear opportunities for increased automation, including deep learning-based segmentation and analysis pipelines to improve scalability and analysis throughput. Sample sizes were modest; however, these animal models and phenotypes were rigorously validated in our prior work,[31,33] and statistically significant differences were consistently observed across groups, underscoring the sensitivity of the imaging and analytical framework. In addition, our analyses focused primarily on structural vascular features and did not incorporate physiological measurements such as blood flow or perfusion, which could further enhance biological interpretation and enable arterial-venous differentiation within the 3D framework. Finally, this study relied on advanced multiphoton imaging to achieve high-resolution, 3D visualization of the retinal vasculature, a modality not currently available in clinical practice. While this limits immediate translation to patients, it enabled the validation of high-fidelity analytical methods using subcellular-resolution datasets in preclinical models that can serve as structural ground truth for future adaptation to clinically accessible imaging modalities, particularly OCT angiography and emerging high-resolution 3D imaging technologies.[53] As retinal imaging continues to evolve toward deeper volumetric analysis, the framework presented here provides a foundational platform that is readily adaptable to research and clinically deployable imaging systems.

This work establishes a comprehensive framework for 3D retinal vascular quantification that extends beyond conventional vessel-level metrics to reveal layer-specific vulnerabilities and network-level architectural principles governing vascular health and disease. Our discovery of convergent ML disruption across mechanistically distinct pathologies, including spontaneous chorioretinal neovascularization and impaired neurovascular patterning, suggests that middle-

386 layer fragmentation may represent a universal structural signature of early retinal vascular
387 instability across a wide range of inciting mechanisms. This interpretation is strengthened by
388 clinical OCTA findings demonstrating that the intermediate capillary plexus shows early and
389 differential vulnerability in diabetic retinopathy,[3,30] and that deeper plexus nonperfusion
390 predicts disease complications independently of superficial layer changes,[36] pointing to a layer-
391 specific hierarchy of vascular resilience that our 3D framework is uniquely positioned to
392 resolve. By resolving true 3D spatial trajectories, inter-plexus connectivity patterns, and layer-
393 specific complexity metrics, this framework captures microarchitectural features that are
394 fundamentally inaccessible to 2D projection-based analyses yet may hold the key to earlier
395 disease detection. The high-resolution anatomical maps generated here serve a dual purpose:
396 first, as discovery tools for identifying which specific architectural features harbor the greatest
397 diagnostic and prognostic value; and second, as quantitative benchmarks for developing
398 algorithms that may detect these same features in lower-resolution but clinically available
399 retinal angiography data. Immediate next steps include systematic validation of vascular
400 biomarkers across expanded disease models, development of automated deep learning
401 pipelines for 3D segmentation and analysis, and prospective evaluation of whether ML
402 fragmentation and inter-plexus geometric distortion provide diagnostic or predictive
403 information in human systemic and neurovascular diseases. As clinical retinal vascular imaging
404 technologies continue their evolution toward higher-resolution volumetric acquisition, the
405 methods and biological insights presented here provide a computational and conceptual
406 foundation for incorporating layer-resolved retinal microvascular analysis into translational
407 and clinical investigation.

408 **Methods**

409 **Animals**

410 All animal procedures were approved by the Laboratory Animal Resource Center at the
411 University of California, San Francisco. Mice were housed in a pathogen-free facility under
412 12-h light/12-h dark cycles with ad libitum access to food and water. For the neovascular model,
413 *Col4a1*$^{+/\Delta ex41}$ mice on C57BL/6J (B6) genetic background were crossed with 129 mice (009104;
414 Jackson Laboratory), which develop spontaneous chorioretinal neovascularization and
415 anastomoses in late adulthood, as previously described.[33] Eyes of both sexes and littermate
416 controls were harvested and prepared for imaging at 8-12 months of age. For the developmental
417 model, Piezo2^{Nts} knockout C57BL/6J mice were used, which exhibit disrupted 3D retinal and
418 cerebellar vascular lattice organization during early and perinatal development, as previously
419 reported.[31] Eyes were harvested at 2 months of age from both sexes as well as littermate controls.

420 **Retinal Vascular Imaging**

421 Mice were anesthetized and transcardially perfused with phosphate-buffered saline (PBS).
422 Whole eyes were harvested and fixed overnight in 4% paraformaldehyde (PFA) at 4°C. Eye
423 specimens were depigmented using 3% H_2O_2 for 2 hours, then washed in PBS for 2 hours with
424 gentle shaking at 37°C. Specimens were incubated with 5 μg/ml Lycopersicon esculentum
425 (Tomato) lectin DyLight 649(Vector Laboratories, ZK0717) for 2 days at 37°C to label the
426 vasculature. Labeled eye specimens were mounted in 1% agarose and imaged using a custom
427 two-photon excited fluorescence microscope (modified Bergamo II, ThorLabs) using 1238 nm
428 excitation light (Insight X3, SpectraPhysics) and a high numerical aperture water-dipping lens
429 (Nikon 25× Apo LWD, 1.10 NA, 2.0 mm WD; THN25X-APO-MP1300) to acquire image data
430 with subcellular resolution. To preserve native 3D retinal vascular architecture, image Z-stacks
431 were acquired directly through the sclera of the intact globe using a 2-μm step size (Fig. 1a).
432 Each Z-stack spanned approximately 358 μm in depth with a lateral pixel size of 1.12 μm,
433 yielding a field of view of approximately 573 × 573 μm². Interactive visualization of 3D
434 vasculature and segmentation was performed using Imaris (10.2.0 Oxford Instruments).

Vascular Network Segmentation

High-resolution image Z-stacks were stored in TIFF format with acquisition metadata. 3D vascular networks were reconstructed using a semi-automated segmentation pipeline comprising preprocessing, automated tracing, and manual validation steps. Raw images were preprocessed through sequential background subtraction, Gaussian filtering, baseline subtraction, median filtering, and deconvolution to enhance signal quality. Surface objects were generated to encompass vascular signal regions, creating masks that minimized noise artifacts. New imaging channels based on these masks were created and converted to the Imaris file format for analysis.

Automated vessel tracing was performed using the Imaris filament tracing algorithm. Traced structures were manually inspected to correct erroneous connections, add undetected vessels, and verify diameter measurements and branching connectivity. Validated 3D networks were manually stratified into anatomically distinct retinal layers: SL, ML, DL, and IP (Supplementary Video S1). Finalized networks were exported as VRML (wrl) 3D model files and accompanying CSV statistics files containing vessel segment lengths, diameters, branching coordinates, and positional data for downstream quantitative analysis. In the Imaris filament framework, vascular networks were represented as graph structures with vertices (discrete points along vessel centerlines) and edges (connections between vertices). Vertices were classified as terminal points (vessel endpoints), branching points (bifurcation or convergence nodes), or intermediate points (nodes along vessel segments). Segments were defined as collections of edges between branching or terminal vertices.

Computational Analysis Pipeline

Following segmentation and validation in Imaris, downstream quantitative analysis was performed using Retina3D Vascular Analyzer, a hybrid Python/R framework designed for accessible and reproducible 3D vascular analysis. The pipeline requires minimal user setup:

users export reconstructed 3D vascular networks from Imaris as VRML (.wrl) model files and CSV statistics files, rename them according to standardized naming conventions (with in-software guidance and documentation provided), and specify the input directory through the graphical interface to initiate analysis. The pipeline then operates in sequential stages: (1) geometry preprocessing, including convex hull computation (scipy.spatial.ConvexHull, Quickhull algorithm) and alpha shape analysis for volume normalization (Python: numpy, scipy, trimesh, pyvista); (2) three-dimensional fractal dimension analysis using the Bouligand–Minkowski morphological dilation method (Python); and (3) statistical analysis comprising full-thickness quantification, layer-resolved fractal analysis, and inter-layer connectivity assessment (R: mgcv, ggplot2, ggpubr, FSA, pracma). Each preprocessing module can also be used independently as a standalone tool for 3D geometric computation or fractal dimension calculation, enabling integration into other analytical workflows. The pipeline supports both interactive analysis through R Shiny dashboards and automated batch processing for reproducible HTML report generation. Complete source code, installation instructions, example datasets, and interactive documentation are available at the project repository (see Code Availability).

Vascular Network Quantification and Analysis

Vascular network architecture was characterized using multiple morphometric and topological parameters derived from validated 3D models (Table 1). All quantitative analyses were performed within standardized 285 × 285 μm regions of interest (ROI), spanning full retinal thickness from choroid to the SL. The ROI dimension represents the x- and y-axis half-widths of the raw data, and regions were selected to avoid edge artifacts and minimize peripheral optical aberrations of the acquisition window.

Vessel density parameters. Vessel number density and branching point density were calculated by normalizing total counts to the ROI or full imaging region convex hull volume. Vessel

volume density was calculated by dividing the total network volume by the ROI or full imaging region convex hull volume. Convex hull volumes were computed from the 3D vascular point cloud using the Quickhull algorithm (scipy.spatial.ConvexHull), providing a standardized tissue occupancy volume for density normalization. These density metrics provide complementary information: number and branching point densities reflect vascular branching complexity, while volume density captures the total vascular space occupancy within the tissue.

Branching architecture and hierarchical organization. Branch levels were assigned using diameter-based classification. Starting from vessel origins (Branch Level 1), segments at each bifurcation were classified hierarchically: smaller-diameter daughter segments received incremented branch levels, while larger-diameter segments maintained parent levels, capturing network organization from major vessels to terminal capillaries. Branching angles were quantified as angular deviation between vessel segments and parent vessel extension direction (Supplementary Fig. S5), reflecting local bifurcation geometry. Specifically, α represents the angle between the two daughter vessel segments extending from the bifurcation point to their distal endpoints, while β captures the angular deviation between the parent vessel's extended centerline direction and each daughter vessel's initial segment (β_1 and β_2), measured at the nearest vertices from the bifurcation point. Together, these metrics characterize both the hierarchical structure and geometric properties of vascular branching patterns, enabling comparative analysis across developmental and neovascular contexts.

Inter-plexus parallelism. Spatial organization between vascular layers was quantified using Generalized Additive Models (GAM) with 3D surface analysis. 3D point clouds representing vessel positions were extracted from each vascular layer (minimum 8 points per layer due to the algorithm requirement). For each layer, a GAM with thin-plate regression splines fitted smooth surfaces to the positional data. Surface normal vectors were computed at 150×150 grid point using numerical gradient estimation followed by L2 normalization. Parallelism between

510 layers was quantified using cosine similarity between corresponding normal vectors, with the
511 superficial layer serving as reference. GAM fitting was performed using the mgcv package in
512 R.[54] Group differences were assessed using non-parametric tests (Wilcoxon rank-sum for two
513 groups, Kruskal-Wallis for multiple groups) appropriate for angular measurements.

514 *Inter-plexus vessel geometry.* For vessels connecting retinal layers, two complementary
515 geometric parameters were quantified. Vessel orientation angles (θ) were calculated relative to
516 the superficial layer reference frame using local vector analysis at each segment (Fig. 4k),
517 characterizing 3D routing patterns and cross-layer connectivity. Excursion ratio was defined as
518 vessel path length divided by vertical span between layers, with values approaching 1
519 indicating direct perpendicular connections and higher values reflecting more tortuous routing.
520 Detailed computational procedures are provided in Supplementary Methods S.M.1.

521 *Fractal dimension analysis.* 3D fractal dimension (3D FD) was computed using the Bouligand–
522 Minkowski morphological dilation method. Vascular objects were iteratively dilated using
523 spheres of increasing radius r (voxel size = 1 unit, corresponding to 0.2 μm absolute resolution
524 based on analyzed mesh resolution), and the resulting influence volume V(r) was computed at
525 each dilation step. The fractal dimension was derived from the negative slope of the linear
526 regression of log V(r) versus log r within the scale-invariant interval (Equation 1,
527 Supplementary Fig. S6). FD was computed using two complementary geometric
528 representations: (1) skeletonized centerlines, capturing branching topology independent of
529 vessel diameter, and (2) surface meshes, reflecting volumetric occupancy and surface
530 irregularity. This dual approach enabled distinction between topological complexity and spatial
531 occupancy. By definition, FD ranges from 0 to 3, with higher values indicating greater
532 structural complexity; values for retinal vascular networks in this study ranged from
533 approximately 1.6 to 2.0. The Bouligand–Minkowski method was selected for its robustness

and sensitivity to subtle architectural changes in biological networks, demonstrating close agreement with theoretical FD values in mathematical benchmarks.[55]

$$FD = 3 - \frac{\log V(r)}{\log r} \quad (1)$$

Statistical Methods

All quantitative analyses were performed on 3D geometric data (CSV files) and reconstructed retinal 3D model files (WRL files) exported from Imaris. Data processing and statistical analyses were implemented in Python 3.10 (with numpy, scipy, trimesh, and pyvista for geometric and fractal computations) and R 4.4.0 (with tidyverse, ggplot2, ggpubr, mgcv, FSA, and pracma for statistical analysis and visualization) using custom scripts (see code availability).

Quantitative readouts included vessel segment length, diameter, tortuosity, branching order, branching angles, vessel density, and fractal dimension. For fractal dimension analysis, both skeletonized centerlines and vascular surface meshes were evaluated using the Bouligand–Minkowski dilation method, enabling complementary assessment of topological versus volumetric complexity. Inter-plexus geometry was assessed by quantifying parallelism and direct bridging connections between plexuses. Complete definitions of all quantification parameters available for retinal vessel network evaluation are provided in Table 1.

Statistical comparisons were conducted using R base and the stats package, for parametric comparisons between two groups, two-tailed Welch's t-tests were applied after verifying normality using Shapiro-Wilk tests. Multi-group comparisons were performed using one-way ANOVA with Tukey's honest significant difference post hoc tests to control for multiple comparisons. Nonparametric alternatives (Wilcoxon rank-sum test for two groups, Kruskal-

556 Wallis test with Dunn's post hoc for multiple groups) were used when normality assumptions
557 were violated or when distributions were non-Gaussian for angular measurements.

558 Sample sizes for each experimental group are reported in the figure legends. All statistical tests
559 were two-sided, with a significance threshold of $\alpha = 0.05$. No adjustments were made for
560 multiple comparisons across different vascular parameters, as each represents an independent
561 biological measurement. Data are presented as mean ± standard deviation unless otherwise
562 noted. Boxplots display median (center line), interquartile range (box bounds), whiskers
563 extending to 1.5× IQR, and outliers as individual points beyond whiskers.

564 Sample sizes were determined based on effect sizes observed in previous studies of retinal
565 vascular pathology and developmental models using these genetic lines,[31,33] and were sufficient
566 to detect statistically significant differences across all primary endpoints. All experiments
567 included littermate controls to minimize genetic background effects.

568 **Vessel Network Terminology**

569 Retinal vascular networks were represented as graph-based filament structures following
570 IMARIS conventions, where vessels are decomposed into vertices (discrete points along vessel
571 centerlines) and edges (connections between adjacent vertices). Vertices were classified by
572 topological position as terminal points (vessel endpoints), branching points (bifurcation or
573 convergence nodes), or intermediate points (nodes along vessel segments), with segments
574 defined as collections of edges between branching or terminal vertices representing individual
575 vessel branches within the network hierarchy. For anatomically specific analyses, vessels were
576 stratified into distinct retinal compartments: superficial layer plexus (SL, ganglion cell layer),
577 middle layer plexus (ML, intermediate capillary plexuses), deep layer plexus (DL, outer
578 plexiform layer), and intermediate plexus (IP, ML with perpendicular vessels linking retinal

layers). This graph-based representation enabled quantitative morphological and topological analysis of complex 3D vascular architectures.

Data Availability

Example datasets for pipeline validation are included in the Retina3D Vascular Analyzer pipeline repository. Additional multiphoton imaging data and processed vascular network models from this study are available upon request.

Code Availability

The Retina3D Vascular Analyzer pipeline (v1.1) is freely available at https://ucsf.box.com/v/Retina3DVascularAnalyzer. The repository includes complete installation guides, example datasets, and interactive user manuals.

Author Contributions:

W.S. designed the study, collected and analyzed the data, developed the computational analysis framework, and wrote the manuscript. G.H. assisted with experiments and data collection. W.E.K. assisted with data analysis and edited the manuscript. R.A.M. helped with analysis and editing the manuscript. P.Z. helped with analysis and editing the manuscript. K.T. collected data and edited the manuscript. X.D. provided key materials, result interpretation, and edited the manuscript. D.B.G. provided key materials, result interpretation, and edited the manuscript. T.N.K. conceived and supervised the study, interpreted results, and wrote the manuscript.

Acknowledgements:

We thank Dr. Frank Tahvi, Mr. Arjun Shivkumar, Dr. Cassandre Labelle-Dumais and Dr. Mao Mao for their intellectual input and discussions. This work was made possible by National Institutes of Health (NEI-K08EY033030, NEI-K12EY031372, NEI-P30EY002162, R01EY030138), BrightFocus Foundation (M2021015N), Research to Prevent Blindness, as well as generous support from the All May See Foundation, Huang Pacific Foundation, and Dr. David and Cecilia Lee.

Competing Interests:

The authors declare no competing interests.

References

1. Fruttiger, M. Development of the retinal vasculature. *Angiogenesis* **10**, 77–88 (2007).
2. Patton, N. *et al.* Retinal vascular image analysis as a potential screening tool for cerebrovascular disease: a rationale based on homology between cerebral and retinal microvasculatures. *J. Anat.* **206**, 319–348 (2005).
3. Fayed, A. E. *et al.* Retinal vasculature of different diameters and plexuses exhibit distinct vulnerability in varying severity of diabetic retinopathy. *Eye* **38**, 1762–1769 (2024).
4. Poplin, R. *et al.* Prediction of cardiovascular risk factors from retinal fundus photographs via deep learning. *Nat. Biomed. Eng.* **2**, 158–164 (2018).
5. Geerling, C. F. *et al.* Changes of the retinal and choroidal vasculature in cerebral small vessel disease. *Sci. Rep.* **12**, 3660 (2022).
6. Cheung, C. Y. *et al.* A deep-learning system for the assessment of cardiovascular disease risk via the measurement of retinal-vessel calibre. *Nat. Biomed. Eng.* **5**, 498–508 (2021).

620 7. Danielescu, C. *et al.* Automated Retinal Vessel Analysis Based on Fundus Photographs as a
621 Predictor for Non-Ophthalmic Diseases—Evolution and Perspectives. *J. Pers. Med.* **14**, 45
622 (2023).
623 8. Liu, Y. *et al.* AI-based 3D analysis of retinal vasculature associated with retinal diseases
624 using OCT angiography. *Biomed. Opt. Express* **15**, 6416–6432 (2024).
625 9. Spaide, R. F., Fujimoto, J. G., Waheed, N. K., Sadda, S. R. & Staurenghi, G. Optical coherence
626 tomography angiography. *Prog. Retin. Eye Res.* **64**, 1–55 (2018).
627 10. Sampson, D. M., Dubis, A. M., Chen, F. K., Zawadzki, R. J. & Sampson, D. D. Towards
628 standardizing retinal optical coherence tomography angiography: a review. *Light Sci. Appl.*
629 **11**, 63 (2022).
630 11. Zahid, S. *et al.* Fractal Dimensional Analysis of Optical Coherence Tomography
631 Angiography in Eyes With Diabetic Retinopathy. *Invest. Ophthalmol. Vis. Sci.* **57**, 4940–4947
632 (2016).
633 12. Durbin, M. K. *et al.* Quantification of Retinal Microvascular Density in Optical Coherence
634 Tomographic Angiography Images in Diabetic Retinopathy. *JAMA Ophthalmol.* **135**, 370–
635 376 (2017).
636 13. Zhang, M. *et al.* Projection-resolved optical coherence tomographic angiography. *Biomed.*
637 *Opt. Express* **7**, 816–828 (2016).
638 14. Kim, T. N. *et al.* Line-Scanning Particle Image Velocimetry: An Optical Approach for
639 Quantifying a Wide Range of Blood Flow Speeds in Live Animals. *PLoS ONE* **7**, e38590
640 (2012).
641 15. Wang, T. Three-photon imaging of mouse brain structure and function through the intact
642 skull. *Nat. Methods* **15**, 9 (2018).

643 16. Qin, Z. *et al.* Adaptive optics two-photon microscopy enables near-diffraction-limited and
644 functional retinal imaging in vivo. *Light Sci. Appl.* **9**, 79 (2020).
645 17. Shih, A. Y. *et al.* Two-Photon Microscopy as a Tool to Study Blood Flow and Neurovascular
646 Coupling in the Rodent Brain. *J. Cereb. Blood Flow Metab.* **32**, 1277–1309 (2012).
647 18. Zhang, J. *et al.* Optical sectioning methods in three-dimensional bioimaging. *Light Sci.*
648 *Appl.* **14**, 11 (2025).
649 19. Rubart, M. Two-photon microscopy of cells and tissue. *Circ. Res.* **95**, 1154–1166 (2004).
650 20. Zhang, Q. *et al.* Retinal microvascular and neuronal pathologies probed in vivo by adaptive
651 optical two-photon fluorescence microscopy. *eLife* **12**, e84853 (2023).
652 21. Hirano, T., Chanwimol, K., Weichsel, J., Tepelus, T. & Sadda, S. Distinct Retinal Capillary
653 Plexuses in Normal Eyes as Observed in Optical Coherence Tomography Angiography Axial
654 Profile Analysis. *Sci. Rep.* **8**, 9380 (2018).
655 22. Tahir, W. *et al.* Anatomical Modeling of Brain Vasculature in Two-Photon Microscopy by
656 Generalizable Deep Learning. *BME Front.* **2020**, 8620932 (2020).
657 23. Zhang, J. *et al.* 3D microvascular reconstruction in retinal OCT angiography images via
658 domain-adaptive learning. *Pattern Recognit.* **165**, 111494 (2025).
659 24. Garrity, S. T., Iafe, N. A., Phasukkijwatana, N., Chen, X. & Sarraf, D. Quantitative Analysis of
660 Three Distinct Retinal Capillary Plexuses in Healthy Eyes Using Optical Coherence
661 Tomography Angiography. *Investig. Opthalmology Vis. Sci.* **58**, 5548 (2017).
662 25. Zudaire, E., Gambardella, L., Kurcz, C. & Vermeren, S. A Computational Tool for Quantitative
663 Analysis of Vascular Networks. *PLOS ONE* **6**, e27385 (2011).

664 26. Narotamo, H., Silveira, M. & Franco, C. A. 3DVascNet: An Automated Software for
665 Segmentation and Quantification of Mouse Vascular Networks in 3D. *Arterioscler. Thromb.*
666 *Vasc. Biol.* **44**, 1584–1600 (2024).
667 27. Bumgarner, J. R. & Nelson, R. J. Open-source analysis and visualization of segmented
668 vasculature datasets with VesselVio. *Cell Rep. Methods* **2**, 100189 (2022).
669 28. Milde, F., Lauw, S., Koumoutsakos, P. & Iruela-Arispez, M. L. The mouse retina in 3D:
670 quantification of vascular growth and remodeling. *Integr. Biol. Quant. Biosci. Nano Macro* **5**,
671 1426–1438 (2013).
672 29. Stahl, A. *et al.* The Mouse Retina as an Angiogenesis Model. *Invest. Ophthalmol. Vis. Sci.* **51**,
673 2813–2826 (2010).
674 30. Haddad, C., Baleine, M. & Motulsky, E. An OCT-A Analysis of the Importance of
675 Intermediate Capillary Plexus in Diabetic Retinopathy: A Brief Review. *J. Clin. Med.* **13**, 2516
676 (2024).
677 31. Toma, K. *et al.* Perivascular neurons instruct 3D vascular lattice formation via neurovascular
678 contact. *Cell* **187**, 2767-2784.e23 (2024).
679 32. Selvam, S., Kumar, T. & Fruttiger, M. Retinal vasculature development in health and disease.
680 *Prog. Retin. Eye Res.* **63**, 1–19 (2018).
681 33. Alavi, M. V. *et al.* Col4a1 mutations cause progressive retinal neovascular defects and
682 retinopathy. *Sci. Rep.* **6**, 18602 (2016).
683 34. Lian, Y., Li, G., Liu, H. & Zhang, Q. Fractal analysis of retinal microvasculature and
684 cardiovascular outcome: a systematic review and meta-analysis. *BMC Ophthalmol.* **25**, 668
685 (2025).

35. Chang, C.-C. *et al.* Three-dimensional Imaging Coupled with Topological Quantification Uncovers Retinal Vascular Plexuses Undergoing Obliteration. *Theranostics* **11**, 1162–1175 (2021).
36. Ong, J. X., Konopek, N., Fukuyama, H. & Fawzi, A. A. Deep Capillary Nonperfusion on OCT Angiography Predicts Complications in Eyes with Referable Nonproliferative Diabetic Retinopathy. *Ophthalmol. Retina* **7**, 14–23 (2023).
37. Nesper, P. L. & Fawzi, A. A. Human Parafoveal Capillary Vascular Anatomy and Connectivity Revealed by Optical Coherence Tomography Angiography. *Invest. Ophthalmol. Vis. Sci.* **59**, 3858–3867 (2018).
38. Zhu, Z. *et al.* Oculomics: Current concepts and evidence. *Prog. Retin. Eye Res.* **106**, 101350 (2025).
39. Wagner, S. K. *et al.* Insights into Systemic Disease through Retinal Imaging-Based Oculomics. *Transl. Vis. Sci. Technol.* **9**, 6 (2020).
40. Wong, T. Y. *et al.* Retinal microvascular abnormalities and 10-year cardiovascular mortality: A population-based case-control study. *Ophthalmology* **110**, 933–940 (2003).
41. Liu, S. *et al.* Beyond the eye: A relational model for early dementia detection using retinal OCTA images. *Med. Image Anal.* **102**, 103513 (2025).
42. Gao, Y. *et al.* A narrative review of retinal vascular parameters and the applications (Part I): Measuring methods. *Brain Circ.* **9**, 121–128 (2023).
43. Campbell, J. P. *et al.* Detailed Vascular Anatomy of the Human Retina by Projection-Resolved Optical Coherence Tomography Angiography. *Sci. Rep.* **7**, 42201 (2017).

44. Arnould, L. *et al.* Using Artificial Intelligence to Analyse the Retinal Vascular Network: The Future of Cardiovascular Risk Assessment Based on Oculomics? A Narrative Review. *Ophthalmol. Ther.* **12**, 657–674 (2023).
45. Zhang, J., Shi, L. & Shen, Y. The retina: A window in which to view the pathogenesis of Alzheimer's disease. *Ageing Res. Rev.* **77**, 101590 (2022).
46. Yao, J., Hong, A. S. Y., Fukutsu, K. & Ting, D. S. W. Artificial intelligence oculomics for systemic health and longevity medicine: 2025 and beyond. *Curr. Opin. Ophthalmol.* **36**, 477–486 (2025).
47. Cheung, C. Y. *et al.* Retinal imaging in Alzheimer's disease. *J. Neurol. Neurosurg. Psychiatry* **92**, 983–994 (2021).
48. Haft-Javaherian, M. *et al.* Deep convolutional neural networks for segmenting 3D in vivo multiphoton images of vasculature in Alzheimer disease mouse models. *PloS One* **14**, e0213539 (2019).
49. Xie, J. *et al.* Deep segmentation of OCTA for evaluation and association of changes of retinal microvasculature with Alzheimer's disease and mild cognitive impairment. *Br. J. Ophthalmol.* **108**, 432–439 (2024).
50. Krohn, S. *et al.* Evaluation of the 3D fractal dimension as a marker of structural brain complexity in multiple-acquisition MRI. *Hum. Brain Mapp.* **40**, 3299–3320 (2019).
51. Labelle-Dumais, C. *et al.* COL4A1 Mutations Cause Ocular Dysgenesis, Neuronal Localization Defects, and Myopathy in Mice and Walker-Warburg Syndrome in Humans. *PLOS Genet.* **7**, e1002062 (2011).

52. Kuo, D. S., Labelle-Dumais, C. & Gould, D. B. COL4A1 and COL4A2 mutations and disease: insights into pathogenic mechanisms and potential therapeutic targets. *Hum. Mol. Genet.* **21**, R97–R110 (2012).

53. Wang, L., Wang, B., Chhablani, J., Sahel, J. A. & Pi, S. Freqformer: Frequency-Domain Transformer for 3-D Reconstruction and Quantification of Human Retinal Vasculature. *IEEE Trans. Biomed. Eng.* 1–11 (2025) doi:10.1109/TBME.2025.3612332.

54. Wood, S. N. Fast Stable Restricted Maximum Likelihood and Marginal Likelihood Estimation of Semiparametric Generalized Linear Models. *J. R. Stat. Soc. Ser. B Stat. Methodol.* **73**, 3–36 (2011).

55. Backes, A. R. & Bruno, O. M. Fractal and Multi-Scale Fractal Dimension analysis: a comparative study of Bouligand-Minkowski method. Preprint at https://doi.org/10.48550/arXiv.1201.3153 (2012).

Figures and legends

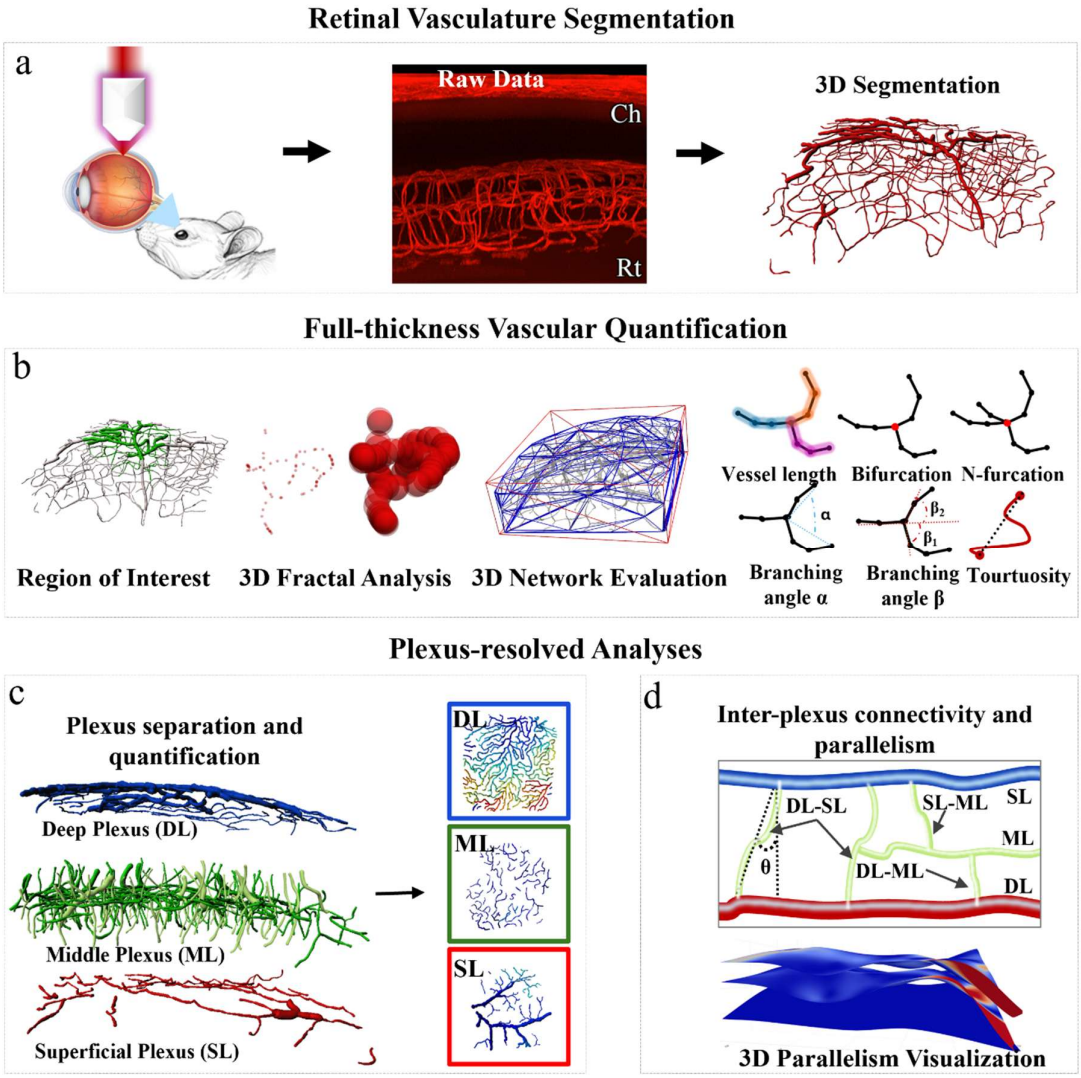

Figure 1. Pipeline for 3D retinal vasculature analysis.

(a) Retinal vasculature segmentation. High-resolution two-photon excitation microscopy Z-stacks spanning the choroid (Ch) and the neurosensory retina (Rt) were acquired. The volumetric data were segmented to generate three-dimensional representations for analysis. **(b)** Full-thickness vascular quantification. Global analyses of vessel morphology and network architecture were performed across the entire vascular volume or within user-defined regions of interest. Quantified parameters include vessel length, diameter, branching angle, tortuosity, vessel volume density, branching topology, network connectivity, and fractal dimension. **(c)** Plexus-resolved analyses. The retinal vasculature was separated into the superficial layer (SL), middle layer (ML), and deep layer (DL) vascular plexuses. Plexus-specific quantification was then performed to characterize layer-dependent vascular architecture. **(d)** Inter-plexus connectivity and parallelism. Cross-plexus relationships were analyzed by characterizing direct inter-plexus connections between SL, ML, and DL and assessing deviation in inter-plexus parallelism.

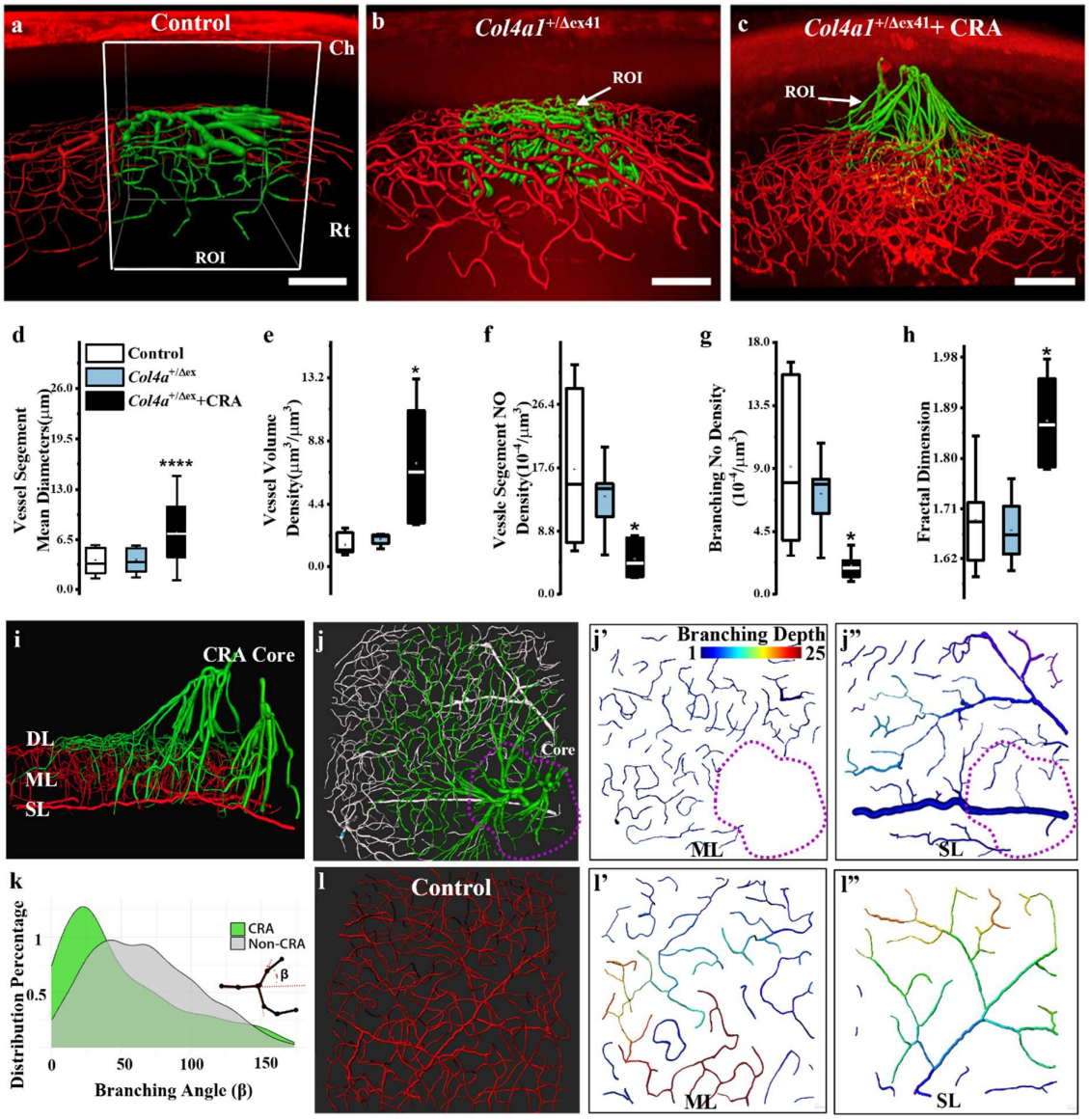

Figure 2. CRA lesions in Col4a1$^{+/\Delta ex41}$ mice are associated with capillary rarefaction, middle-layer loss, and radial vessel orientation.

(a) Representative 3D reconstruction of control retina showing intact trilaminar vasculature organization. The white cube indicates the standardized 285 × 285 μm analysis window spanning the choroid (Ch) to the superficial layer plexus (SL). **(b)** Representative *Col4a1*$^{+/\Delta ex41}$ retina without neovascularization, demonstrating preserved laminar organization. **(c)** Representative *Col4a1*$^{+/\Delta ex41}$ retina with chorioretinal anastomosis (*Col4a1*$^{+/\Delta ex41}$+CRA), showing disruption of trilaminar organization and aberrant vessels spanning the choroid and retina. For panels (a-c), vessels within ROI are highlighted in green. Scale bar, 100 μm. **(d)** Mean vessel segment diameter, **(e)** vessel-volume density, **(f)** vessel-number density, and **(g)** branching-point density, all quantified in full-thickness ROIs. **(h)** 3D fractal dimension (Bouligand–Minkowski method), reflecting network space-filling complexity. For analysis in panels **(d-h)**, one ROI was measured per retina per animal (n = 6 controls, n = 5 *Col4a1*$^{+/\Delta ex41}$

without CRA, n = 6 *Col4a1*$^{+/\Delta ex41}$+CRA). Boxplots display the median (center line and interquartile range (Q1-3); whiskers represent 1.5 × IQR; outliers are shown individually. One-way ANOVA with Tukey's post hoc test (* indicates $p < 0.05$; **** indicates $p < 0.0001$; ns, not significant). (i–j") Characterization of CRA lesion. **(i)** Representative 3D reconstruction of a CRA illustrating layer-specific vascular alterations. The deep layer (DL) plexus extends abnormally toward and fuses with the choroid, the middle layer (ML) plexus shows regional depletion and discontinuity, and the superficial layer (SL) plexus appears relatively preserved. **(j)** En face projection of the same CRA lesion with demarcation of the CRA core by a purple dotted contour, wherein there is loss of the ML and radial convergence of vessels toward the lesion center. **(j')** Branching-level map of the ML demonstrating significant network fragmentation, rarefaction, and absence of vessels within the CRA core. The color scale denotes number of connected branches within each grouping of vessels. **(j")** Branching-level map of the SL within the same CRA demonstrating a continuous capillary network, with vessels oriented toward the lesion center. **(k)** Branching-angle analysis. Schematic defining bifurcation branching angle (β) defined as angle deviation from parent vessel trajectory. Within the CRA, the β distribution shifts toward smaller angles compared with non-CRA regions. (l-l') Matched control retina. **(l)** En face projection of a littermate control retina showing a normal vascular network. **(l')** Local branching-level map of the ML in a control retina, demonstrating normal network continuity and branching. **(l'')** Local branching-level map of the SL in a control retina, demonstrating preserved network organization without radial orientation.

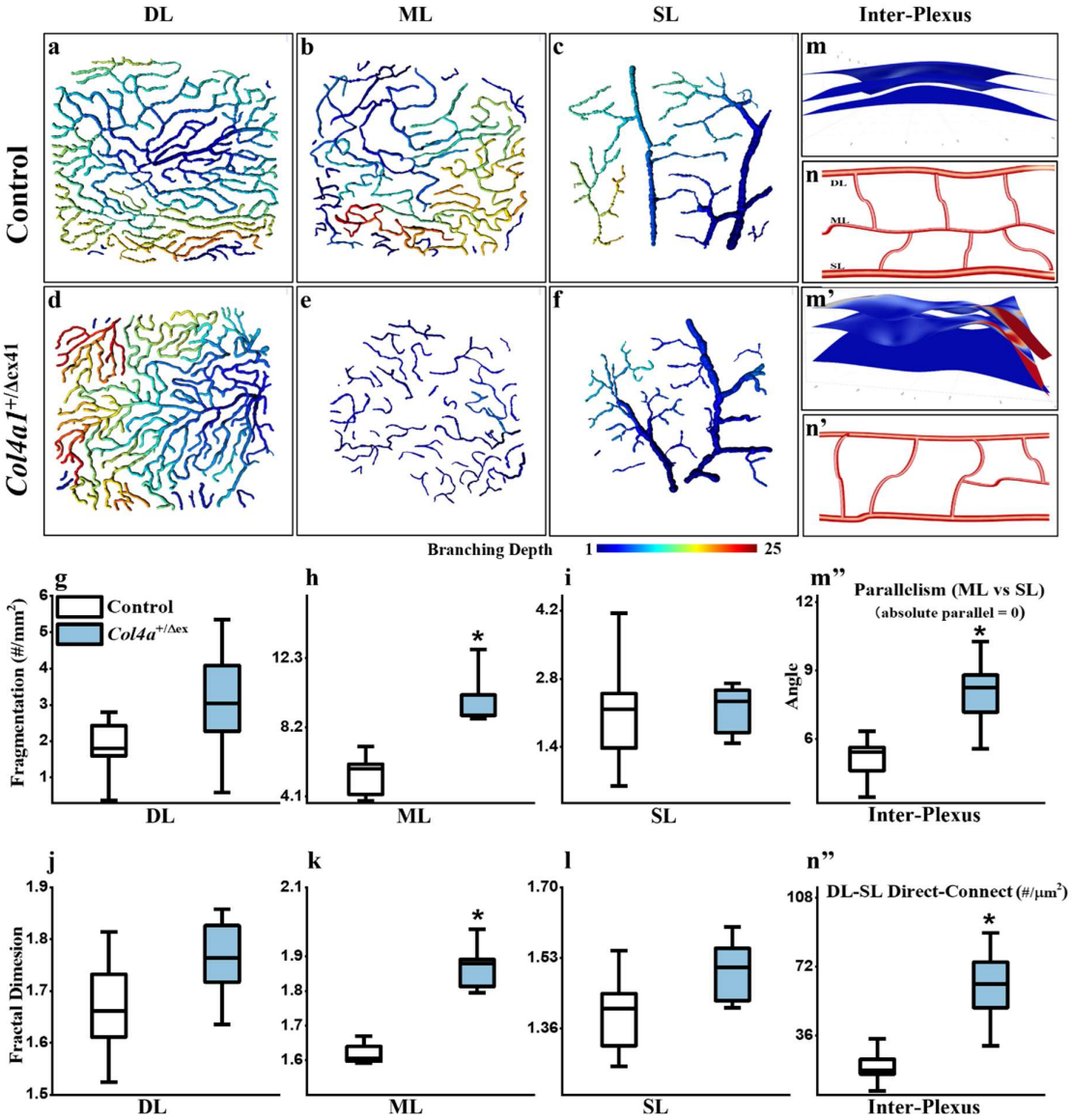

Figure 3. Middle-layer remodeling in Col4a1$^{+/\Delta ex41}$ mice without overt CRA.

(a–c) Plexus-resolved vascular reconstructions from control retina showing deep (DL) (a), middle (ML) (b), and superficial (SL) (c) plexuses. All layers exhibit continuous, interconnected vessel architecture. Color scale denotes number of connecting branches within each grouping of vessels. **(d–f)** Corresponding plexus-resolved reconstructions from Col4a1$^{+/\Delta ex41}$ retina without CRA showing DL (d), ML (e), and SL (f). The ML exhibits discontinuity and fragmentation into isolated vascular segments, whereas DL and SL remain comparatively preserved. **(g–i)** Fragmentation index for DL (g), ML (h), and SL (i), defined as the number of connected vascular networks normalized to analyzed area (see Methods). ML fragmentation is significantly increased in Col4a1$^{+/\Delta ex41}$ retinas (h), whereas DL and SL show no significant change (g, i). **(j–l)** Plexus-specific 3D fractal dimension (FD) for DL (j), ML (k), and SL (l). ML FD is significantly altered in Col4a1$^{+/\Delta ex41}$ retinas (k), whereas DL and SL show no significant change (j,l). Box plots (g-l) show median and interquartile range (Q1–Q3);

whiskers represent 1.5 × IQR; n = 6 control and n = 5 Col4a1$^{+/\Delta ex41}$ retinas; two-tailed Welch's t-test; * indicates $p < 0.05$. **(m–m″)** Inter-plexus parallelism. **(m)** Representative point-wise parallelism heatmap from control retina showing alignment of ML and DL relative to SL, where cooler colors indicate greater parallelism (cosine similarity approaching 1). Spatial heatmaps and 3D surface visualizations are provided in Supplementary Fig. S2. **(m′)** Representative Col4a1$^{+/\Delta ex41}$ retina demonstrating reduced layer parallelism. **(m″)** Quantification of mean inter-plexus parallelism expressed as angular deviation from perfect alignment (0° = perfect parallel). ML–SL parallelism is significantly reduced in Col4a1$^{+/\Delta ex41}$ retinas; DL–SL parallelism is not significantly changed (n = 6 retinas per group; * indicates $p < 0.05$). **(n)** Schematic illustrating inter-plexus connections which typically include the ML in control retina. **(n′)** Schematic illustrating inter-plexus connections in Col4a1$^{+/\Delta ex41}$ retina with increased number of direct DL–SL connections. **(n″)** Number of DL–SL direct connections is substantially increased in Col4a1$^{+/\Delta ex41}$ retinas. Symbols indicate mean; error bars show ± standard error (SE) with caps indicating the 5th–95th percentiles; n = 6 control and n = 5 Col4a1$^{+/\Delta ex41}$ retinas; two-tailed Welch's t-test; * indicates $p < 0.05$.

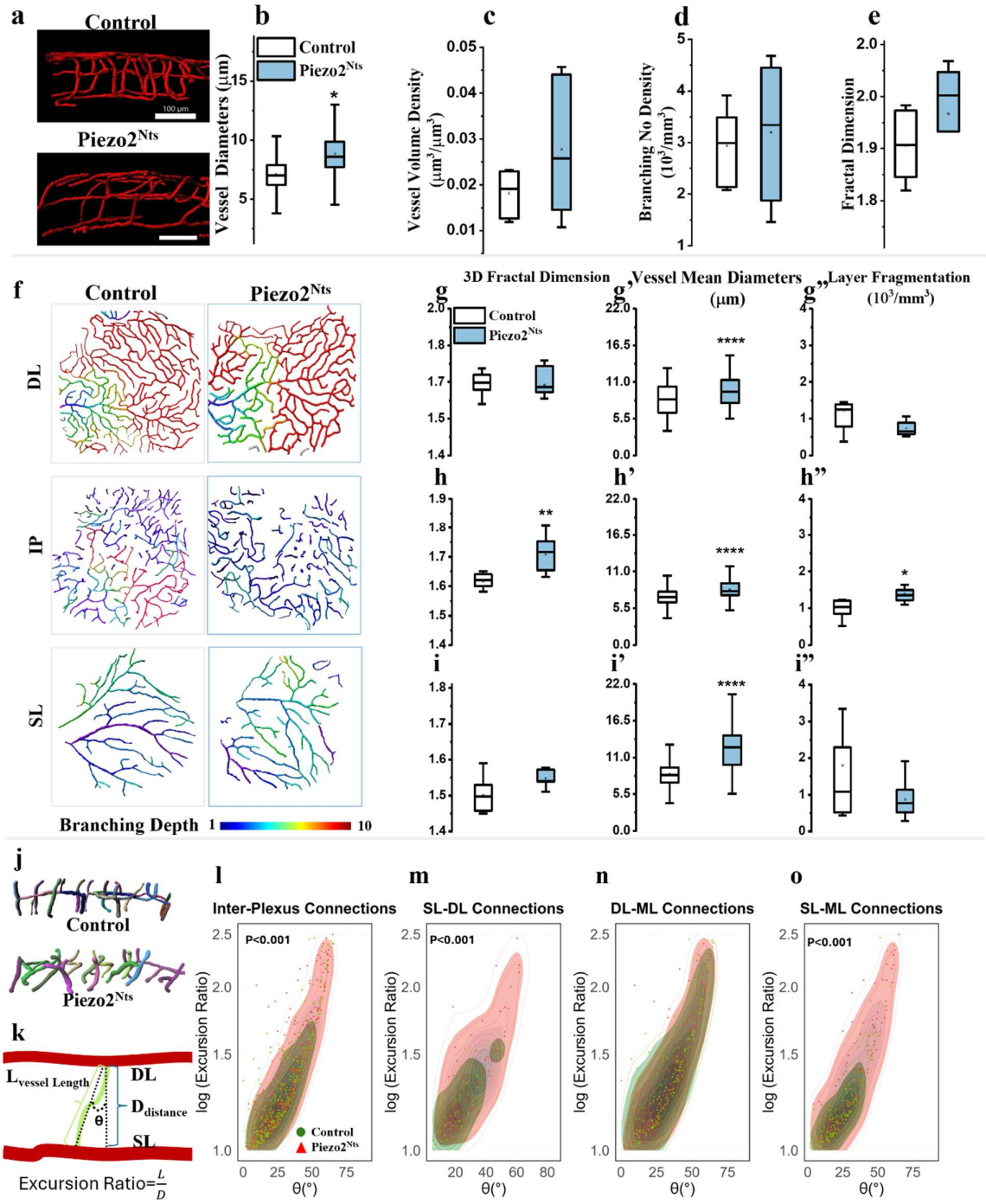

Figure 4. Neuron-specific loss of Piezo2 causes intermediate plexus fragmentation and altered penetrating vessel orientation and connectivity.

(a) Representative side-view projections of full-thickness vasculature from Control and Piezo2^{Nts} retinas. While trilaminar vascular organization remains present in both groups,

Piezo2^{Nts} retinas exhibit irregularities within the intermediate plexus. Scale bars, 100µm. **(b–e)** Full-thickness retinal analyses including: mean segment diameter (b), vessel-volume density (c), branching-point density (d), and 3D fractal dimension (FD; Bouligand–Minkowski method) (e). Full-thickness network analyses detect only modest but significant increases in mean diameter and global 3D FD of Piezo2^{Nts} retinas, with nonsignificant changes in branching and volume densities. Boxplots display median (center line), interquartile range (box), whiskers (1.5 × IQR), and individual outliers. n = 12 retinas per genotype (one Z-stack per retina). Two-tailed Welch's t-test; *, $p < 0.05$; **, $p < 0.01$; ***, $p < 0.001$; ****, $p < 0.0001$. **(f)** Representative vascular reconstructions of the deep layer (DL) plexus, intermediate layer plexus (IP), and superficial layer (SL) plexus in Control and Piezo2^{Nts} retinas. Color scale denotes number of connecting branches within each grouping of vessels. **(g-g'')** DL analyses including 3D FD (g), mean segment diameter (g'), and fragmentation index (g''), demonstrating no statistically significant differences between Control and Piezo2^{Nts} retinas within the DL. **(h-h'')** IP analyses including 3D FD (h), mean segment diameter (h'), and fragmentation index (h''). The IP demonstrates higher 3D FD and mean segment diameter in Piezo2^{Nts} retinas compared with Controls. **(i-i'')** SL analyses, including 3D FD (i), mean segment diameter (i'), and fragmentation index (i''), showing no significant differences between groups. Boxplots as in (b–e). Two-tailed Welch's t-test; *, $p < 0.05$; **, $p < 0.01$; ***, $p < 0.001$; ****, $p < 0.0001$. **(j)** Representative reconstructions of the IP highlighting altered penetrating vessel orientation in Piezo2^{Nts} retinas compared with Controls. **(k)** Schematic describing penetrating vessel characteristics including excursion ratio and orientation angle θ. **(l–o)** Joint distributions of $\log_{10}$(Excursion ratio) vs θ (degrees) for IP vessels including all IP vessels (l), SL–DL direct connections (m), DL–ML direct connections (n), and SL–ML direct connections (o). Piezo2^{Nts} retinas exhibit increased excursion ratio and larger θ, which are more pronounced among SL–ML and SL–DL and direct connecting vessels. *P*-values from Welch's tests.